Sequential transitions of bathtub vortex flow

Jiro Mizushima and Kazuki Abe
Department of Mechanical Engineering, Doshisha University, Kyotanabe, Kyoto 610-0321, Japan

Naoto Yokoyama
Department of Aeronautics and Astronautics, Kyoto University, Kyoto 615-8540, Japan
(Received 20 February 2017; published 23 August 2017)

The bathtub vortex has been found to autonomously arise owing to instability of a symmetric flow in a rectangular vessel when water is drained. We consider a model flow through a vessel with a rectangular horizontal cross section and a drain hole at the center of the bottom to investigate the physical mechanism for generation of swirling fluid motion like the bathtub vortex and the sequential transitions of the flow by numerical simulations and the linear stability analyses. The water surface is assumed to be flat even after instability. If the flow becomes unstable under this assumption, it assures that the surface deformation is irrelevant to the instability. It is emphasized that our interest is not limited to the real bathtub vortex but directed to occurrence of a large vortex in a flow having two reflectional symmetries. The configuration of the vessel has the double plane symmetry (DPS), which allows the flow have the same DPS at small Reynolds numbers. It is found that the instabilities and hence transitions occur accompanying symmetry-breaking of the flow field. Namely, the DPS flow experiences instability to yield vortical motion above a critical Reynolds number, losing the DPS but retaining the π-rotational (twofold rotational) symmetry around the center axis. The vortical flow also becomes unstable at a higher Reynolds number, makes a transition, and loses the π-rotational symmetry, but still keeps the time-translation symmetry, i.e., steadiness. The steadiness is broken at an even higher Reynolds number, owing to instability caused by an oscillatory mode of disturbance. The first and second transitions of the flow are identified as pitchfork bifurcations, and the third transition is identified as a Hopf bifurcation.

DOI: 10.1103/PhysRevFluids.2.083903

I. INTRODUCTION

In our everyday lives, we often get sight of vortical fluid motions, among which the vortex appearing above a drain hole of washbowls, kitchen sinks, and bathtubs attracts our interest. A popular belief is that the vortex swirls counterclockwise in the Northern Hemisphere and clockwise in the Southern Hemisphere. It was Shapiro's motivation to determine the validity of the widespread belief. He performed experiments [1] to reveal the effect of Earth's rotation on the formation process of the bathtub vortex. In his experiments, he used a cylindrical vessel and took care to prevent noises and disturbances, which break the axisymmetry of the experimental apparatus. His experiments showed that the bathtub vortex swirled in the counterclockwise direction nine times out of ten in Boston. Subsequent experiments repeated in Australia [2] also confirmed the effect of Earth's rotation showing that the bathtub vortex swirled in the clockwise direction.

The generation mechanism of the bathtub vortex has long been investigated by the use of circular vessels based on the assumption that the whole system has the axisymmetry [3–6], and its structure has also been studied in detail [7–10]. Here, the axisymmetric system is referred to as the system that has both the zero circumferential derivatives of physical quantities of the flow and the axisymmetric boundary conditions.

Numerical simulation has an advantage over experiments to exclude miscellaneous factors such as imperfection of the shape of the vessel, inclination in the base setting, inhomogeneous temperature distribution in the water, and most importantly, residual angular momentum in water. When the

system has axisymmetry, the numerical simulation gave more definite conclusions on the formation mechanism of the bathtub vortex than experiments [11]. It was clarified that the bathtub vortex is transiently formed by gathering residual angular momentum that remained when the drain is pulled open, if the whole system is set on a stationary ground. Thus, angular momentum must be supplied to make a steady bathtub vortex [12]. On the other hand, when the whole system rotates, a vortex that has the same swirl direction with system's rotation appears owing to the Coriolis force after decay of the transient vortex due to the residual angular momentum. It was proved that the formation of the bathtub vortex in the axisymmetric system is not related to instability or bifurcation. The shape of the vessel is crucial for the formation of the bathtub vortex and also for the determination of swirl direction of the vortex.

The transition or instability of flow is usually accompanied by symmetry breaking [13]. The relation between the bifurcations and the symmetries of the system has been widely formulated [14,15]. If the emergence of the bathtub vortex is attributable to the instability of flow that accompanies any spatial symmetry-breaking, it must be a consequence of the pitchfork bifurcation. Through a pitchfork bifurcation, the flow makes a transition from a steady state with some spatial symmetries into another steady state by losing one spatial symmetry. This transition is caused by instability due to growth of disturbance having antisymmetry with respect to the broken symmetry. On the other hand, a Hopf bifurcation arises when the flow field loses its time-translation symmetry. In this case, time-periodic disturbances grow to cause flow oscillations.

In fact, the formation mechanism of the bathtub vortex was once predicted to be instability of the flow without any vortical motion by experiments [16,17] in a noncylindrical vessel, where a vessel having a rectangular cross section was adopted, though an octagonal shape of percolator is set to suppress disturbances in the central region. The experimental result was quite different from the case of the cylindrical vessel, suggesting that the emergence of the bathtub vortex is a critical phenomenon. It was confirmed in numerical simulations that the bathtub vortex is certainly induced by instability when the flow rate is larger than a threshold [18] if the flow does not have the axisymmetry but has a double plane symmetry. It was also shown that the transition from the double-plane symmetric flow having no bathtub vortex to the bathtub vortex flow is caused by a pitchfork bifurcation, where even a small perturbation can determine the swirl direction of the bathtub vortex. Moreover, the pitchfork bifurcation is known to be structurally unstable, and an imperfect pitchfork bifurcation appears instead if any factor of perturbation which breaks its symmetry is added to the system. Therefore, the Coriolis force can determine the swirl direction to be cyclonic. In a rectangular vessel, once the swirling motion arises, the swirling motion is accelerated autonomously by self-excitation cycles through the pressure acting on the side walls. The acceleration of the angular momentum is brought only by the pressure on the side walls, if the Coriolis force is not applied. It was also shown that the pressure distribution is caused by two secondary vortices adjacent to the side walls. Then, the locations of the secondary vortices as well as the symmetries of the flow play an important role to maintain the bathtub vortex.

It is anticipated that the bathtub-vortex flow in the rectangular vessel would become unstable again and make transitions into oscillatory flow eventually. We reconsider the instability of the flow through a vessel with a rectangular cross section taking the same configuration as our previous paper [18], and pursue further transitions of the flow by numerical simulations and the linear stability analyses in the present paper. The water surface is assumed to be flat even after a vortical motion is induced. This assumption assures that the surface deformation is irrelevant to the generation mechanism of the bathtub vortex if instability occurs on the assumption. Our concern is not limited to the real bathtub vortex but directed to more general instabilities occurring in a flow that has two reflectional symmetries. We will discuss the instabilities and transitions relating symmetry breaking up to three sequential transitions in the Reynolds number range of $\mathrm{Re} \leqslant 300$. The transition to the oscillatory flow appearing at $\mathrm{Re} \approx 280$ is discussed only qualitatively, because it is confirmed only by the numerical simulations with a coarser grid than required to assure sufficient numerical accuracy.

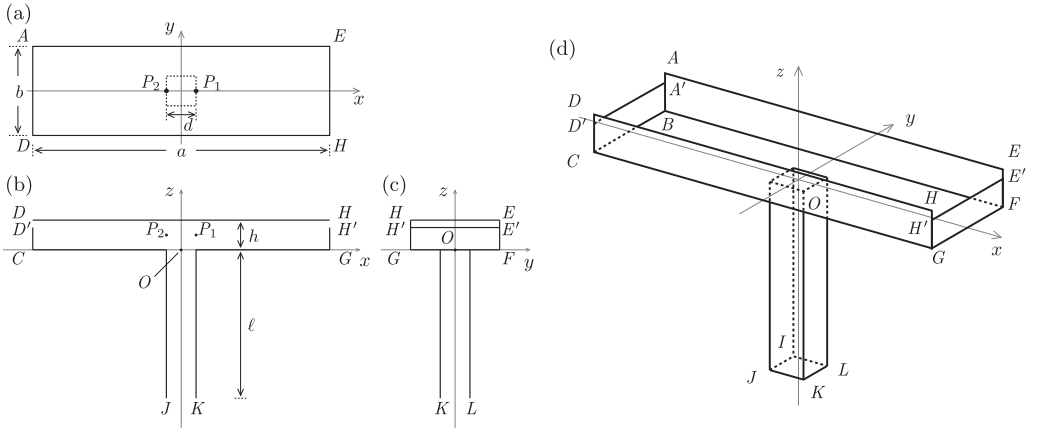

FIG. 1. Computational model of the bathtub. (a) top view, (b) front view, (c) side view, and (d) bird view.

This paper is organized as follows. The formulation and numerical scheme for numerical simulations and linear stability analyses are given in Sec. II. The numerical results are shown in Sec. III. The last section is devoted to the summary and discussion.

II. FORMULATION AND NUMERICAL SCHEME

A. Governing equations and boundary conditions

We consider the flow in a container consisting of a rectangular vessel and a square drain pipe attached to the drain hole located at the center of the bottom as shown in Fig. 1. Water inflows through the two inlets $AA'D'D$ and $EE'H'H$, goes through the rectangular vessel and the drain pipe, and outflows through the outlet $IJKL$. The origin O is placed at the center of the drain hole, and the x and y axes are taken parallel to each pair of side walls on the horizontal bottom, while the z axis is vertically upward. The side length of the square drain hole is expressed by d, and the sides of the rectangular vessel are $a = 10d$ and $b = 3d$ in the x and y directions. The height of the solid wall normal to the y axis is taken to be larger than d to keep the water level $h = d$, while the side walls normal to the x axis are set to be $3d/4$ to allow water come through between the top of the walls and the water level. The water surface is assumed to be flat, being nondeformable. The length of the drain pipe is $\ell = 5d$. Two points, indicated by $P_1(d/2,0,d/2)$ and $P_2(-d/2,0,d/2)$ in Fig. 1, are the representative points chosen to characterize the flow field by using the y-component velocities at the locations.

The flow is assumed to be incompressible and viscous. The side length d of the square outlet and the mean outflow velocity in the z direction $W = Q/d^2$ at the outlet are employed as the characteristic length and velocity scales, respectively, where Q is the outflow volumetric flux per unit time. Using the characteristic length and velocity scales we make all physical quantities nondimensional and define the Reynolds number as $\mathrm{Re} = Q/(\nu d)$ with d, W and the kinematic viscosity of water ν. Then, the time is made nondimensional with d/W and pressure with ρW^2. From now on, we will use only nondimensional variables. For example, both the nondimensional depth and the side length of the drain hole is 1 in terms of nondimensional variables, since the water level h is taken to be equal to d. The governing equations for the nondimensional velocity $\boldsymbol{u} = (u,v,w)$ and the pressure p, the incompressible Navier-Stokes equation and the continuity equation, are expressed as

$$\nabla \cdot \boldsymbol{u} = 0, \quad \frac{\partial \boldsymbol{u}}{\partial t} + (\boldsymbol{u} \cdot \nabla)\boldsymbol{u} = -\nabla p + \frac{1}{\mathrm{Re}}\Delta \boldsymbol{u}. \tag{1}$$

The gravity is incorporated into the pressure term, so that the external force due to gravity does not appear in Eq. (1). The typical MAC method is used to numerically solve Eq. (1) as an initial-value and boundary-value problem.

The parabolic profile in the y direction of the x component of velocity and vanishing y and z velocity components,

$$u = \mp\left\{1 - \left(\frac{2y}{3}\right)^2\right\}, \quad v = 0, \quad w = 0 \quad \text{for } x = \pm 5, \quad 3/4 < z \leqslant 1, \tag{2}$$

are employed for the boundary condition on the inlets $AA'D'D$ and $EE'H'H$. The boundary condition for the pressure is given to satisfy the Navier-Stokes equation on the inlets as

$$\frac{\partial p}{\partial x} = -u\frac{\partial u}{\partial x} + \frac{1}{\mathrm{Re}}\left(\frac{\partial^2 u}{\partial x^2} + \frac{\partial^2 u}{\partial y^2}\right). \tag{3}$$

The boundary condition on the outlet is the natural outflow condition:

$$\frac{\partial u}{\partial z} = 0, \quad \frac{\partial v}{\partial z} = 0, \quad \frac{\partial w}{\partial z} = 0. \tag{4}$$

The pressure is set to 0 over the whole outlet cross-section. Another boundary condition where the pressure is set to 0 only at the center of the outlet is confirmed to give the same flow fields within seven significant digits in numerical results.

On the flat water surface, the slip condition,

$$\frac{\partial u}{\partial z} = 0, \quad \frac{\partial v}{\partial z} = 0, \quad w = 0, \tag{5a}$$

$$\frac{\partial p}{\partial z} = \frac{1}{\mathrm{Re}}\frac{\partial^2 w}{\partial z^2}, \tag{5b}$$

is used, and the water height is assumed to be constant. The nonslip condition,

$$u = 0, \quad v = 0, \quad w = 0, \tag{6}$$

is used on all the solid boundaries. The boundary condition for p is given in terms of the normal velocity component u_n and the normal coordinate n to each solid boundary as

$$\frac{\partial p}{\partial n} = \frac{1}{\mathrm{Re}}\frac{\partial^2 u_n}{\partial n^2}. \tag{7}$$

In numerical calculations, including numerical simulations, calculation of the steady flows, and linear stability analyses, we adopt a uniformly distributed staggered grid with the same finite difference in the x, y, and z spatial coordinates, $\Delta x = \Delta y = \Delta z = \Delta h = 0.03125$. The second-order central difference is used for the spatial derivatives. In solving the Navier-Stokes equation, the Euler method with a time step $\Delta t = 2\times 10^{-3}$ is used for the time integration. The initial conditions of the velocity field at small Reynolds numbers are taken to have the double plane symmetry (DPS). That is, the flow field is symmetric with respect to the $x = 0$ plane and the $y = 0$ plane at the initial time. On the other hand, the initial conditions at large Reynolds numbers, where the bathtub vortex is formed, are taken from the velocity field at slightly smaller Reynolds numbers than those under examination. The Poisson equation for the pressure is solved with the successive over relaxation (SOR) method taking the acceleration parameter $\epsilon = 1.2$–1.4.

To verify the numerical accuracy of the numerical simulation results, the horizontal velocity (u_1, v_1), the z component of vorticity ω_1 at the point P_1, and the total angular momentum with respect to the z axis L_z are compared for different grid spacings $\Delta x = \Delta y = \Delta z = \Delta h$ and time steps Δt. We take one example of $\mathrm{Re} = 100$ to examine the numerical accuracy, where the flow attains a steady state having the π-rotational symmetry with the bathtub vortex. The magnitudes of

TABLE I. Accuracy assessment of numerical simulations. Re = 100, steady states ($t = 800$). The relative error ϵ in each physical quantity is evaluated based on the value for the case of $\Delta h = 0.025$. $A = 10/3$. u_1: x component of velocity at P_1, v_1: y component of velocity at P_1, ω_1: z component of vorticity at P_1, L_z: total angular momentum with respect to the z axis.

Δh	Δt	u_1	v_1	ω_1	L_z
0.025	2×10^{-3}	-3.083×10^{-1}	2.397×10^{-1}	6.101×10^{-1}	1.386
ϵ	–	–	–	–	–
0.03125	2×10^{-3}	-3.064×10^{-1}	2.410×10^{-1}	6.083×10^{-1}	1.393
ϵ	–	0.598%	0.559%	0.302%	0.530%
0.05	5×10^{-3}	-3.017×10^{-1}	2.462×10^{-1}	5.967×10^{-1}	1.418
ϵ	–	2.13%	2.70%	2.21%	2.30%

u_1, v_1, ω_1, and L_z are tabulated in Table I. The comparison of these physical quantities between numerical results with $\Delta h = 0.025$ ($\Delta t = 2\times10^{-3}$) and 0.03125 ($\Delta t = 2\times10^{-3}$) confirms that the numerical results with $\Delta h = 0.025$ are accurate within 1% relative errors. Thus, we mainly employ the grid spacing $\Delta h = 0.03125$ and the time step $\Delta t = 2\times10^{-3}$ for the numerical simulations. The details of the formulation and numerical scheme are found in our previous paper [18].

B. Linear stability analysis and flow symmetries

The boundary conditions of the flow having the DPS allow the solution to possess the same DPS at small Reynolds numbers, but the solution originally having the DPS makes transitions to lose the symmetries one by one in sequential experience of instability. Here, we introduce three operators to denote the symmetry breaking: reflections with respect to the $x = 0$ plane and the $y = 0$ plane, M_x ($(x,y,z) \to (-x,y,z)$) and M_y ($(x,y,z) \to (x,-y,z)$), and the π rotation around the z axis, $R_{z\pi}$ ($(x,y,z) \to (-x,-y,z)$). The π-rotation operation is expressed as $R_{z\pi} = M_y \times M_x$, which leads to $M_y = M_x \times R_{z\pi}$. Namely, one reflection operation M_y is equivalent to the sequential operation made of the π-rotation operation $R_{z\pi}$ followed by the other reflection operation M_x.

The flow is eventually attracted to the steady state having the DPS at small Reynolds numbers, being invariant under the operations M_x and M_y, and also invariant under $R_{z\pi}$. The DPS is also interpreted as the composition of the π-rotational (twofold rotational) symmetry around to the z axis (RS) and one plane symmetry with respect to the $x = 0$ or $y = 0$ plane. Thus, if the system has the DPS, the system necessarily has the RS, but the RS does not always imply the DPS.

The DPS flow is the basic flow for the first linear stability analysis, which may become unstable to a disturbance that has the antisymmetry under the operations M_x and M_y above a critical Reynolds number. It is noted that the unstable DPS solutions can be obtained with the SOR method numerically, or even in numerical simulations of the governing Eq. (1) if the DPS is imposed to the velocity and pressure, assuming as

$$u(x,y,z) = u(x,-y,z) = -u(-x,y,z), \quad v(x,y,z) = -v(x,-y,z) = v(-x,y,z),$$
$$w(x,y,z) = w(x,-y,z) = w(-x,y,z), \quad p(x,y,z) = p(x,-y,z) = p(-x,y,z). \tag{8}$$

The first equality in each equation in Eq. (8) shows invariance under M_y, and the equality of the leftmost side with the rightmost side expresses invariance under M_x, while the second equality indicates the RS. The resultant flow arising from the first instability is the bathtub vortex flow, which keeps the RS though the DPS is lost. The RS flow turns out to be the basic flow for the second linear stability analysis, which becomes unstable to a disturbance that has the antisymmetry under the operation $R_{z\pi}$ at Reynolds numbers larger than another critical value. Such basic flows possessing RS are obtained again with the SOR method or in numerical simulations by imposing

the RS:

$$u(x,y,z) = -u(-x,-y,z), \quad v(x,y,z) = -v(-x,-y,z),$$
$$w(x,y,z) = w(-x,-y,z), \quad p(x,y,z) = p(-x,-y,z), \tag{9}$$

on the solutions.

The linear stability analysis assumes a small disturbance $\hat{\boldsymbol{u}}$ and $\hat{p}$ added to the basic flow $\bar{\boldsymbol{u}}$ and $\bar{p}$, which may have the DPS, the RS, or no spatial symmetry, and the velocity $\boldsymbol{u}$ and the pressure p are expressed as the summation of the basic solution and the disturbance, i.e., $\boldsymbol{u} = \bar{\boldsymbol{u}} + \hat{\boldsymbol{u}}$ and $p = \bar{p} + \hat{p}$, respectively. Substituting these expressions to the governing Eq. (1), subtracting the equation for the basic-flow solution and omitting the nonlinear terms of the disturbance, the linear disturbance equation for $(\hat{\boldsymbol{u}}, \hat{p})$ is obtained as

$$\nabla \cdot \hat{\boldsymbol{u}} = 0, \quad \frac{\partial \hat{\boldsymbol{u}}}{\partial t} + (\hat{\boldsymbol{u}} \cdot \nabla)\bar{\boldsymbol{u}} + (\bar{\boldsymbol{u}} \cdot \nabla)\hat{\boldsymbol{u}} = -\nabla \hat{p} + \frac{1}{\mathrm{Re}} \Delta \hat{\boldsymbol{u}}. \tag{10}$$

Usually, $\hat{\boldsymbol{u}}$ and $\hat{p}$ is assumed to have exponential time dependence as $\hat{\boldsymbol{u}} = \widetilde{\boldsymbol{u}} e^{\lambda t}$ and $\hat{p} = \widetilde{p} e^{\lambda t}$ with a complex constant λ in the linear stability theory. Then, Eq. (10) is expressed as

$$\nabla \cdot \widetilde{\boldsymbol{u}} = 0, \quad \lambda \widetilde{\boldsymbol{u}} = -(\widetilde{\boldsymbol{u}} \cdot \nabla)\bar{\boldsymbol{u}} - (\bar{\boldsymbol{u}} \cdot \nabla)\widetilde{\boldsymbol{u}} - \nabla \widetilde{p} + \frac{1}{\mathrm{Re}} \Delta \widetilde{\boldsymbol{u}}. \tag{11}$$

If the real part of λ, $\mathrm{Re}[\lambda]$, is positive, the basic flow is unstable, and stable if $\mathrm{Re}[\lambda] < 0$. The imaginary part of λ, $\mathrm{Im}[\lambda]$, indicates the oscillation frequency of the disturbance.

The boundary conditions for $\hat{\boldsymbol{u}}$ or $\widetilde{\boldsymbol{u}}$ are the same with Eqs. (4), (5a), and (6) for $\boldsymbol{u}$. Because no disturbance is assumed to flow in, $\hat{\boldsymbol{u}} = 0$ on the inlets [see Eq. (2)]. The pressure boundary conditions for $\hat{p}$ or $\widetilde{p}$ is derived from Eqs. (10) or (11), similarly to Eqs. (5b) and (7) in the numerical simulations. The pressure gradient on the inlets ($x = \pm 5$, $3/4 < z \leqslant 1$) is expressed as

$$\frac{\partial \hat{p}}{\partial x} = -\bar{u} \frac{\partial \hat{u}}{\partial x} + \frac{1}{\mathrm{Re}} \frac{\partial^2 \hat{u}}{\partial x^2}. \tag{12}$$

Although there exist infinite eigenvalues and eigen functions each set of which is called a mode, we are interested in the most unstable mode having the largest real part of λ. We adopt the time integration scheme in solving Eq. (10) with the typical MAC method to find the most unstable mode similarly to the numerical simulations of Eq. (1) rather than solving Eq. (11) with the SOR method. To numerically solve Eq. (10) as an initial-value problem, the time derivative is approximated with the Euler method and the spatial derivatives with the second-order central difference for the time integration, and the Poisson equation solver is the same as the numerical simulations of Eq. (1). In the case where the most unstable mode is stationary, the eigen value λ is a real value. Then, we take an appropriate initial condition $(\hat{\boldsymbol{u}}^{(0)}, \hat{p}^{(0)})$ for $(\hat{\boldsymbol{u}}, \hat{p})$, which we normalize to be $\hat{v}_1^{(0)} = 1$ at P_1, calculate the velocity field $(\hat{\boldsymbol{u}}^{(1)}, \hat{p}^{(1)})$ at the next time step $t = \Delta t$ and then normalize them to be $\hat{v}_1^{(1)} = 1$ again. The growth rate $\mathrm{Re}[\lambda^{(0)}]$ is evaluated by $\ln(\hat{v}_1^{(1)}/\hat{v}_1^{(0)})/\Delta t$. If repetition of this procedure leads to a convergent series of $(\hat{\boldsymbol{u}}^{(n)}, \hat{p}^{(n)})$ and $\mathrm{Re}[\lambda^{(n)}]$, then the converged flow field is the eigen function $(\widetilde{\boldsymbol{u}}, \widetilde{p})$ and the converged value of $\mathrm{Re}[\lambda^{(n)}]$ gives the eigen value of $\mathrm{Re}[\lambda]$. For oscillatory modes of disturbance, the solution technique for stationary disturbances cannot be applied, so that numerical simulation of Eq. (10) is easier to calculate the most unstable mode of eigenvalue and eigen function, where the solution $(\hat{\boldsymbol{u}}^{(n)}, \hat{p}^{(n)})$ shows periodic oscillation in time after a long elapse of time. During the time evolution of numerical data, we take two successive local maximum values of $v_1^{(n)}$ and $v_1^{(n+m)}$ at $t = n\Delta t$ and $(n+m)\Delta t$ and calculate the growth rate by $\mathrm{Re}[\lambda^{(n)}] = \ln(\hat{v}_1^{(n+m)}/\hat{v}_1^{(n)})/(m\Delta t)$. If $\mathrm{Re}[\lambda^{(n)}]$ converges toward a value, it is the real part of eigenvalue $\mathrm{Re}[\lambda]$ and the solution $(\hat{\boldsymbol{u}}^{(n)}, \hat{p}^{(n)})$ is the real parts of the eigen function $(\widetilde{\boldsymbol{u}}, \widetilde{p})$. The imaginary part of λ is evaluated by $\mathrm{Im}[\lambda] = 2\pi/(m\Delta t)$, and the imaginary part of the eigen functions are given by $(-\hat{\boldsymbol{u}}^{(n+m/4)}, -\hat{p}^{(n+m/4)})$ because the imaginary part appears $3\pi/4$ rad late in the phase behind the real part. We normalize the complex eigen function $(\widetilde{\boldsymbol{u}}, \widetilde{p})$ to be $\widetilde{v}_1 = 1$.

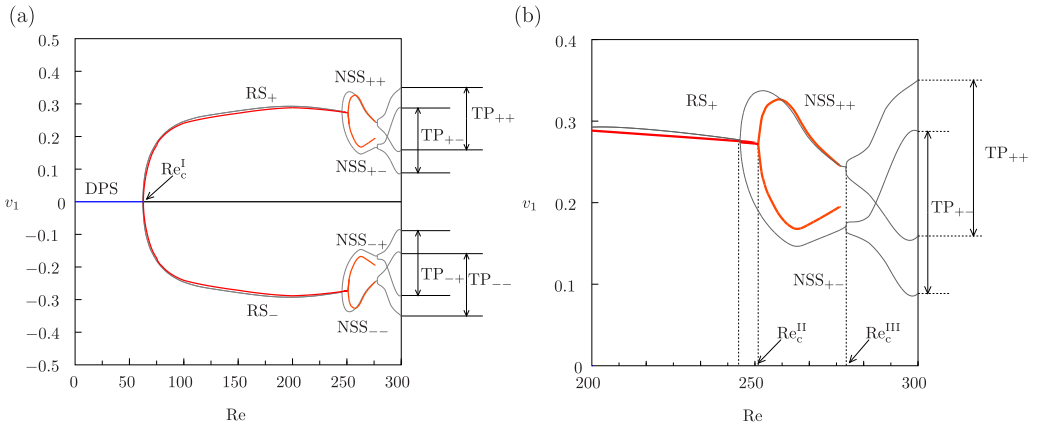

FIG. 2. (a) Bifurcation diagram in $0 \leqslant \mathrm{Re} \leqslant 300$, and (b) enlargement of (a). v_1: y component of velocity at points P_1 (=(1/2,0,1/2)). The diagrams in $0 \leqslant \mathrm{Re} \leqslant 275$ are drawn with two grid spacings $\Delta h = 0.03125$ and $\Delta h = 0.05$. The diagram in $275 \leqslant \mathrm{Re} \leqslant 300$ is drawn only with a grid spacing $\Delta h = 0.05$.

III. NUMERICAL RESULTS

A. Bifurcation and symmetry-breaking

We have performed numerical simulations in the range of $\mathrm{Re} \leqslant 300$ and found that the flow exhibits different properties not only quantitatively but also qualitatively as the Reynolds number increases. The qualitative change of flow indicates transitions from one state to another, each of which accompanies a change in the number of solutions for the fundamental equations. Each origin of the transitions will be explored by the linear stability analysis in the next subsection. Such transitions of flow are depicted by a bifurcation diagram as shown in Fig. 2, where the y-component velocity $v_1 = v(P_1)$ at P_1 (=(1/2,0,1/2)) indicated in Fig. 1 is used to characterize the flow field. The velocity v_1 can be substituted by v_2 at P_2 (=(−1/2,0,1/2)) if the double plane symmetry (DPS) or the π-rotational symmetry around the z axis (RS) is considered as explained later. Note that only stable solutions are drawn while unstable solutions are omitted in Fig. 2.

The thick and thin lines in Figs. 2(a) and 2(b) indicate numerical results obtained by using the fine grid spacing $\Delta h = 0.03125$ and the coarse grid spacing $\Delta h = 0.05$, respectively. We assert the numerical accuracy of the bifurcation diagram indicated by the thick lines from the fine grid simulation, but the numerical simulations in the fine grid requires too much computation time beyond our tolerance to pursue extension of the diagram to larger Reynolds numbers than $\mathrm{Re} = 275$ with accuracy within 1% in the relative error, so that simulation results in the coarser grid are added to supplement the bifurcation structure. The similarity of the two diagrams supports the correctness of both numerical results.

The solution branch along $v_1 = 0$ indicated by DPS is the only solution for $\mathrm{Re} < \mathrm{Re}_c^{\mathrm{I}}$, having the DPS without any vortical motion. At $\mathrm{Re} = \mathrm{Re}_c^{\mathrm{I}}$, two other solution branches having finite values of v_1, emerge from the DPS solution with $v_1 = 0$, which indicates emergence of a bathtub vortex. The positive value of v_1 comes from the existence of a bathtub vortex swirling in the counterclockwise. Since the system's configuration has the DPS, once the flow with the counterclockwise swirling bathtub vortex is observed, its counterpart having a vortex in the clockwise rotation could appear instead. Then, the whole DPS would be preserved, which is reflected on the bifurcation diagram. Thus, two branches RS_+ and RS_- appear. The abbreviation RS represents that the flow field has the π-rotational symmetry [Eq. (9)], and the signs + and −, respectively, represent $v_1 > 0$ and $v_1 < 0$. The swirling direction of the bathtub vortex is not uniquely determined theoretically but chosen by a slight asymmetry included in the vessel configuration or residual angular momentum remaining in water when the water drain begins. Therefore, the bifurcation diagram is symmetric with respect

TABLE II. Accuracy assessment of numerical simulations. The relative errors ϵ in the critical Reynolds numbers are evaluated by comparing the values with those for $\Delta h = 0.03125$.

Δh	Δt	$\mathrm{Re}_c^{\mathrm{I}}$	$\mathrm{Re}_c^{\mathrm{II}}$
0.03125	2×10^{-3}	62.81	251.01
ϵ	–	–	–
0.05	5×10^{-3}	62.24	245.25
ϵ	–	0.907%	2.29%

to the Re axis. The first critical Reynolds number is determined as $\mathrm{Re}_c^{\mathrm{I}} = 62.81$, and the relation $v_1^2 \propto (\mathrm{Re} - \mathrm{Re}_c^{\mathrm{I}})$ holds near the critical Reynolds number. The relation shows that the bifurcation is a pitchfork bifurcation at $\mathrm{Re}_c^{\mathrm{I}}$. It is added that in the case where the whole system is rotating, the pitchfork bifurcation is degenerated into an imperfect one owing to structural instability [18]. Then, the bathtub vortex that appears will have the same swirling direction as the rotation of the system, i.e., cyclonic, unless residual disturbance is so large to surpass the imperfection.

Another bifurcation occurs at $\mathrm{Re}_c^{\mathrm{II}} = 251.01$, which turns out to be another pitchfork bifurcation. Four branches of steady solutions, NSS_{++}, NSS_{+-}, NSS_{-+}, and NSS_{--}, stem from the bifurcation points owing to the instability at $\mathrm{Re} = \mathrm{Re}_c^{\mathrm{II}}$, where the abbreviation NSS stands for no spatial symmetries. Although the NSS flows have no spatial symmetries, the bifurcation diagram in Fig. 2 is symmetric with respect to the Re axis. This symmetry is inherited from RS before the bifurcation at $\mathrm{Re}_c^{\mathrm{II}}$. If any flow solution on the NSS_{++} branch has the value of v_1, then the magnitude of v_2 on the NSS_{++} branch is equal to v_1 on the NSS_{-+} branch, for instance. Thus, the two solution NSS_{-+} and NSS_{--} are, respectively, obtained from NSS_{++} and NSS_{+-} by the π rotation around the z axis, when v_1 is exchanged with v_2.

The accuracy of the numerical simulations are assessed here again in terms of the critical Reynolds numbers for the two pitchfork bifurcations. The critical values of $\mathrm{Re}_c^{\mathrm{I}}$ and $\mathrm{Re}_c^{\mathrm{II}}$ are evaluated on the computation grids with $\Delta h = 0.03125$ and 0.05 and tabulated in Table II. Both the relative errors ϵ in the first critical Reynolds number $\mathrm{Re}_c^{\mathrm{I}}$ and the second $\mathrm{Re}_c^{\mathrm{II}}$ are smaller than 2.5%. Therefore, we confirm that the numerical accuracy is enough to resolve the small-scale flows even for the instability phenomena.

The flow is always oscillatory for $\mathrm{Re} > \mathrm{Re}_c^{\mathrm{III}}$. The solution branches of the oscillatory flow have not been completely obtained in numerical simulations with $\Delta h = 0.03125$ but with a coarser grid of $\Delta h = 0.05$ as displayed in the bifurcation diagram (Fig. 2). The transition from steady to oscillatory flow is the third bifurcation, which is found to be a Hopf bifurcation, and the critical Reynolds number is determined as $\mathrm{Re}_c^{\mathrm{III}} = 278.0$, though $\mathrm{Re}_c^{\mathrm{III}}$ is expected to become a little larger in more precise results. The time-periodic solutions are referred to as TP_{++}, TP_{+-}, TP_{-+}, and TP_{--} in the bifurcation diagram (Fig. 2), each corresponding to one of the four NSS branches in $\mathrm{Re}_c^{\mathrm{II}} < \mathrm{Re} < \mathrm{Re}_c^{\mathrm{III}}$. The abbreviation TP represents that the flow field is time-periodic. These branches satisfy the same spatial symmetries as NSS_{++}, NSS_{+-}, NSS_{-+}, and NSS_{--} expressed in Eq. (14).

We will show the physical implication in the sequential transitions, investigating the instability phenomena from the viewpoint of the symmetry breaking. The flow has the DPS at small Reynolds numbers, an example of which is shown for $\mathrm{Re} = 60$ in Figs. 3(a) and 3(b). Figure 3(a) shows streamlines and isosurfaces of ω_z. The streamlines are drawn as traces of fluid particles which inflow through the line segment of $x = \pm 5$ and $z = 7/8$. The fluid particles come toward the drain hole centripetally, and outflow from the outlet through the drain pipe, where each group of particles coming from the opposite side of $x = 5$ and -5 outflow through each distinct region of $x > 0$ or $x < 0$ at the outlet, never mingling with each other and showing no emergence of bathtub vortex. Four regions of relatively large vorticity, depicted by isosurfaces in Fig. 3(a), spread from the inlets to near the drain

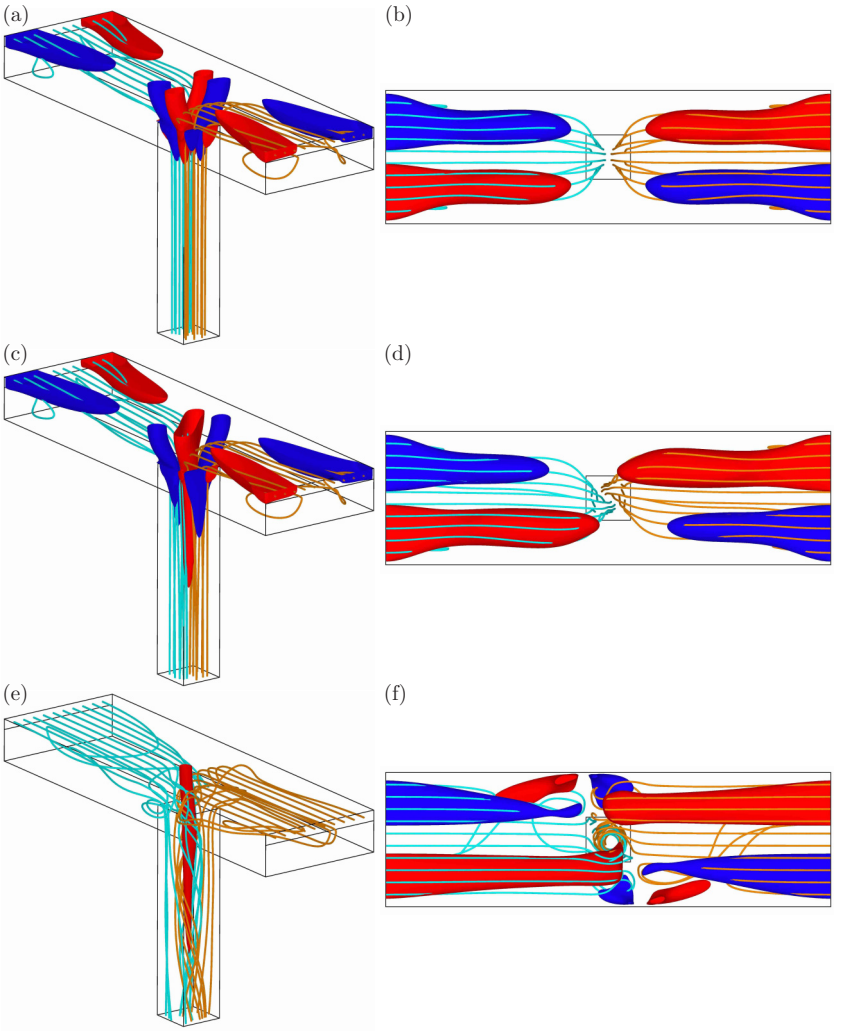

FIG. 3. Flow fields at Re = 60 ((a) and (b), DSP), Re = 65 ((c) and (d), RS_+), and Re = 260 ((e) and (f), NSS_{++}). Streamlines passing inward from the segment $x = \pm 5$ and $z = 7/8$ are drawn. Isosurfaces of ω_z are drawn in (a), (c), (e) (bird view), and isosurfaces of l_z in (b), (d), and (f) (top view). (a), (c) $\omega_z = 0.5$ (red) and $\omega_z = -0.5$ (blue). (b), (d) $l_z = 0.15$ (red) and $l_z = -0.15$ (blue). (e) $\omega_z = 8$ (red). (f) $l_z = 0.3$ (red) and $l_z = -0.3$ (blue).

hole, each pair of the isosurfaces of ω_z with the opposite sign facing to the other antisymmetrically. Here, we note that the vorticity at the inlets ($x = \pm 5$) is given as $\omega_z \approx -\partial u/\partial y = \mp 8y/9$ and that the signs of isosurfaces of ω_z are negative in the regions of $xy > 0$ and positive in $xy < 0$. Two more couples of tubular large-vorticity regions are observed to spread from the water surface above the drain hole into the drain pipe, whose signs are also negative in the regions $xy > 0$ and positive in $xy < 0$.

The isosurfaces of the z-component local angular momentum per unit volume $l_z = \pm 0.15$ are drawn together with streamlines in Fig. 3(b), where l_z is defined by $l_z = xv - yu$. Similarly to the large-vorticity regions, four regions of large magnitude of l_z spread from the inlets. Note that the angular momenta are $l_z = \pm y\{1 - (2y/3)^2\}$ on the inlets ($x = \pm 5$) and they are positive in the region of $xy > 0$ and negative in $xy < 0$, contrary to ω_z. The angular momentum decays to 0 when

the fluid particles approach the drain hole. The DPS that the angular momentum distribution shows confirms the absence of any bathtub vortex at this Reynolds number as well.

At $\mathrm{Re} = 65$, a slightly larger value than $\mathrm{Re}_c^{\mathrm{I}}$, a steady bathtub vortex appears above the drain hole and also within the drain pipe as shown in Figs. 3(c) and 3(d). Differently from the no-vortex flow for $\mathrm{Re} < \mathrm{Re}_c^{\mathrm{I}}$, the fluid particles coming through the inlets exhibit swirling motions around the drain hole before leaving from the outlet as the streamlines show in Fig. 3(c). The two positive large-vorticity regions, having been located in the domains of $xy < 0$ at $\mathrm{Re} = 60$, merge with each other at $\mathrm{Re} = 65$. The merged large-vorticity region is flattened in the diagonal direction across the drain hole and drained into the drain pipe forming an elongated column. On the other hand, the negative large-vorticity regions are not so different from those at $\mathrm{Re} = 60$.

The isosurfaces of l_z are shown for $\mathrm{Re} = 65$ in Fig. 3(d), which clearly shows breaking of the DPS and only the π-rotational symmetry around the z axis (RS) remains. The RS assures the coincidence of the axis of the bathtub vortex with the center line of the drain hole. As explained in Sec. II B, only two of three symmetries, i.e., the two plane symmetries and the RS, are independent. Because the RS remains while the two plane symmetries with respect to the $x = 0$ and $y = 0$ planes are broken, the bifurcation at $\mathrm{Re} = \mathrm{Re}_c^{\mathrm{I}}$ are regarded as a single symmetry-breaking. Therefore, the bifurcation at $\mathrm{Re} = \mathrm{Re}_c^{\mathrm{I}}$ is confirmed to be a pitchfork bifurcation also in terms of the symmetry consideration.

The flow field depicted in Figs. 3(c) and 3(d) is the solution manifested by a point at $\mathrm{Re} = 65$ on the RS_+ branch ($v_1 > 0$) in the bifurcation diagram (Fig. 2), while its counterpart on the RS_- branch ($v_1 < 0$) is obtained by reflection with respect to the $x = 0$ or $y = 0$ plane. This consequence comes from breaking of the DPS in each individual solution, while the whole system must keep the DPS after bifurcation, which yields the counterpart of the solution that lost the DPS. The relation between the flow field (u_+, v_+, w_+, p_+) on the RS_+ branch and (u_-, v_-, w_-, p_-) on the RS_+ branch is expressed as

$$u_-(x,y,z) = u_+(x,-y,z) = -u_+(-x,y,z), \tag{13a}$$

$$v_-(x,y,z) = -v_+(x,-y,z) = v_+(-x,y,z), \tag{13b}$$

$$w_-(x,y,z) = w_+(x,-y,z) = w_+(-x,y,z), \tag{13c}$$

$$p_-(x,y,z) = p_+(x,-y,z) = p_+(-x,y,z). \tag{13d}$$

The second equality on each in Eq. (13) holds owing to the RS of the flow fields on each of the RS_+ and RS_- branches. Because of the symmetry Eq. (13b), the value of v_2, which is the y-component velocity at P_2, of the solution on the RS_+ branch is equal to that of v_1 on the RS_- branch. Discussion on the flow field on the RS_- branch is omitted because it is reproduced by reflecting the solution on the RS_+ branch in Figs. 3(c) and 3(d) with respect to the $x = 0$ plane or the $y = 0$ plane.

As shown in Fig. 2, the second bifurcation occurs at $\mathrm{Re}_c^{\mathrm{II}} = 251.01$. The flow pattern at $\mathrm{Re} = 260$ (Figs. 3(e) and 3(f), NSS_{++}) is more complex than that of $\mathrm{Re} = 65$ [Figs. 3(c) and 3(d)], where the streamlines twist around the large-vorticity region before they outflow. The axis of the bathtub vortex does not coincide with the z axis. Affected by the secondary vortices appearing near the side walls at $y = \pm 3/2$, some streamlines draw complex trajectories before getting entangled into the bathtub vortex. Although the isosurface of $\omega_z = 8$ is visible in Fig. 3(e), no portion of isosurface of $\omega_z = -8$ appears because negative vorticity is weaker than $|\omega_z| = 8$. The tubular large-vorticity region near the z axis has a core apart from the z axis lying in the domain of $x > 0$ and $y < 0$. Thus, the RS of the flow field is broken, and the flow field has no spatial symmetries at $\mathrm{Re} = 260$.

The broken RS is obvious in the l_z distribution in Fig. 3(f). Only the positive large-angular-momentum tube spreading from a domain of $y < 0$ at the inlet $x = -5$ reaches the drain hole, while the other tube coming from the domain of $y > 0$ at the inlet $x = 5$ ends before arriving the drain hole, though the distinction may not be clear in this figure. The asymmetry is prominent in the shape of the secondary vortices with positive l_z near the side walls at $y = \pm 3/2$; the upper left one is much longer and thicker than the lower right counterpart located diagonally in Fig. 3(f). Therefore, another pitchfork bifurcation is found to appear at $\mathrm{Re} = \mathrm{Re}_c^{\mathrm{II}}$, out of breaking of the RS. The flow

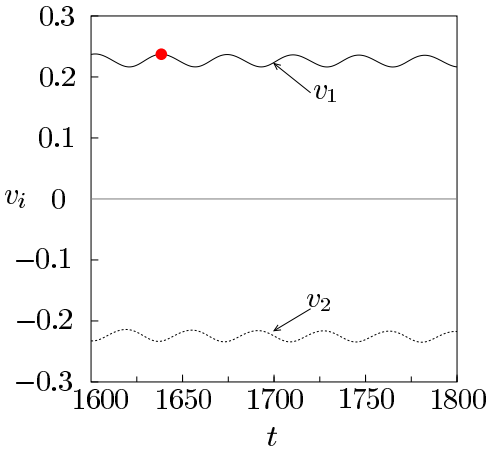

FIG. 4. Time evolution of the y-component velocities v_1 at $P_1 = (1/2,0,1/2)$ and v_2 at $P_2 = (-1/2,0,1/2)$. $\mathrm{Re} = 285$. The point at $t = 1638.4$ denotes the time at which the flow field is drawn in Fig. 5.

field has no spatial symmetry at $\mathrm{Re} > \mathrm{Re}_c^{\mathrm{II}}$, but reserves the time-translation symmetry, i.e., the steadiness.

Although there exist four stable solutions at $\mathrm{Re} = 260$ in Fig. 2 only the flow field of NSS_{++} is shown in Figs. 3(e) and 3(f). Another solution on the NSS_{+-} branch in Fig. 2, can be obtained by the π-rotation operation with respect to the z axis of the NSS_{++} solution. This is also the reason that the broken RS in the individual solution must be compensable allowing the counterpart to keep the RS as a whole. Thus, the solution on the NSS_{+-} branch is expressed in terms of that on the NSS_{++} branch as

$$\begin{aligned} u_{+-}(x,y,z) &= -u_{++}(-x,-y,z), \quad v_{+-}(x,y,z) = -v_{++}(-x,-y,z), \\ w_{+-}(x,y,z) &= w_{++}(-x,-y,z), \quad p_{+-}(x,y,z) = p_{++}(-x,-y,z), \end{aligned} \tag{14}$$

where the suffixes $++$ and $+-$, respectively, represent the NSS_{++} and the NSS_{+-} branches. The solutions on the NSS_{-+} branch and the NSS_{--} branch are, respectively, obtained by the reflection operation with respect to the plane of $x = 0$ or $y = 0$ of that on the NSS_{+-} branch and the NSS_{++} branch, similar to the relation between the RS_+ and RS_- branches at the first bifurcation. Therefore, the value of v_2 on the NS_{++} (NS_{+-}) branch is equal to that of v_1 on the NS_{-+} (NS_{--}) branch.

The oscillatory flow is confirmed to certainly appear at $\mathrm{Re} = 285$ with the finer grid of $\Delta h = 0.03125$, and the time evolutions of the velocity components v_1 at P_1 and v_2 and P_2 are depicted in Fig. 4, in which the periodic time series clearly shows that the time-translation symmetry is broken. The time period in the oscillation is approximately 37.6. Because the mean values of v_1 and v_2 are approximately 0.223 and -0.227, respectively, the mean circumferential velocity on the circle that passes P_1 and P_2, $x^2 + y^2 = (1/2)^2$ and $z = 1/2$, is evaluated as 0.225. The characteristic time for one circulation of the bathtub vortex on the circle with its center at the z axis passing through P_1 and P_2 is estimated as 14.0. Thus, the period of the variation of the flow field is roughly three times longer than the characteristic time of circulation of the bathtub vortex.

Since the flow field varies periodically in time, the streamlines and the isosurfaces of $\omega_z = 8$ are drawn for an instant of the solution on the NSS_{++} branch at $\mathrm{Re} = 285$ in Fig. 5. The instant, $t = 1638.4$, is chosen because v_1 has the maximal value at the moment. Although the flow field at $t = 1657.2$, when v_1 attains to its minimum, is omitted, the differences between the flows at $t = 1638.4$ and at $t = 1657.2$ appear only in the locations and the strengths of the vortex. Both flows show a thin tubular large-vorticity region along the z axis and streamlines twist

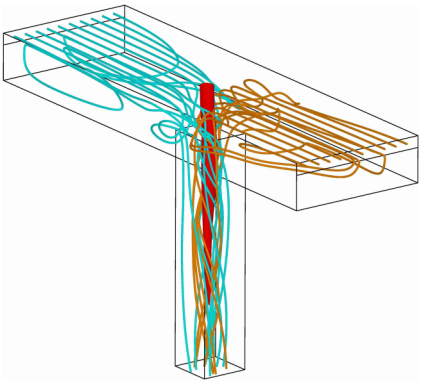

FIG. 5. Isosurfaces of $\omega_z = 8$ at $t = 1638.4$ when v_1 is maximal at $\mathrm{Re} = 285$ on TP_{++}. Streamlines passing inward from the segment $x = \pm 5$ and $z = 7/8$, and isosurfaces of ω_z are drawn.

around the large-vorticity region as shown in Fig. 5 similarly to the flow at $\mathrm{Re} = 260$ shown in Figs. 3(e) and 3(f).

The second bifurcation was brought by a slight shift of the vortex center to the lower right or the upper left from the z axis as shown in Fig. 6. The third bifurcation occurs when the center of the vortex oscillates back and forth in the diagonal direction with a very small amplitude accompanying oscillation in the vortex strength. This oscillation of the vortex center and strength yields the

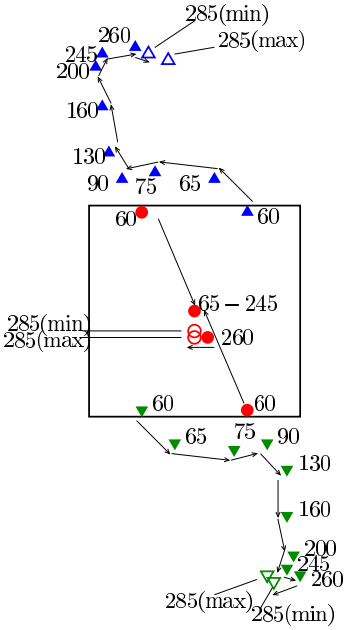

FIG. 6. Locations of maximal and (locally) minimal ω_z on the $z = 1/2$ plane. The x axis is directed to the right and the y axis upward with the origin being the center. The maximal locations and the (locally) minimal locations are, respectively, represented by circles and triangles. Solid symbols and open symbols respectively represent steady flows at $\mathrm{Re} < \mathrm{Re}_c^{\mathrm{III}}$ and oscillatory flow at $\mathrm{Re} = 285 > \mathrm{Re}_c^{\mathrm{III}}$. The locations of the maximal and locally minimal ω_z at the instant when v_1 peaks at its maximum and minimum in the oscillatory flow at $\mathrm{Re} = 285$ are indicated by 285 (max) and 285 (min), respectively. Only the domain $|x|, |y| \leqslant 3/2$ is drawn.

oscillatory flow, or vice versa. When v_1 attains the largest (smallest) value, the magnitude of v_2 is also most (least) negative. Thus, the variations of v_1 and v_2 are synchronous in the oscillatory bathtub-vortex flow.

To observe the spatial symmetries of the flow field and their breakings more clearly, locations of the maxima and (local) minima of ω_z on the plane $z = 1/2$ are drawn for several Reynolds numbers in Fig. 6, where the x axis is directed to the right and the y axis upward with the origin being the center. At $\mathrm{Re} = 60$ ($<\mathrm{Re}_c^{\mathrm{I}}$), the two positive maxima on the plane appear above the opposing corners of the drain hole, and the two minima having a negative value emerge above the other opposing corners. The absolute values of the two maxima and the two minima are the same. The DPS is clearly confirmed by the alignment of the maxima and minima of ω_z.

The two maxima, having been located above the opposing corners at $\mathrm{Re} = 60$, come to the center with formation of the bathtub vortex and coalesce into one on the z axis at $\mathrm{Re} = 65 > \mathrm{Re}_c^{\mathrm{I}}$. As Re increases, the minimum in the $y > 0$ side changes its location to the negative x direction (to the left in Fig. 6), and the other minimum in the $y < 0$ side to the positive x direction. The change of the locations of the two minima are caused by the vortical flow that swirls stronger for larger Re in the counterclockwise direction. At $\mathrm{Re} \approx 90$, each of the two minima reaches almost above the opposite corner of the drain hole and turns toward the side wall. This change of direction is brought by the colliding streams of the vortical flow and the main flow coming from the inlets to the drain hole. During the increase in Re up to $\mathrm{Re}_c^{\mathrm{II}}$, the two minima are always located in the diagonal direction, and the maximum stays on the z axis. The two minima have the same negative value, whose absolute value is smaller than the maximum. Thus, the RS is confirmed also by the alignment of the maximum and the minima.

The values of the two minima differ and their locations deviate from the diagonal line across the z axis for $\mathrm{Re} > \mathrm{Re}_c^{\mathrm{II}}$. The local minimum in the region of $y > 0$ drifts to the positive x direction along the side wall at $\mathrm{Re} \approx 260$ while the counterpart in $y < 0$ does not move so much at $\mathrm{Re} \gtrapprox 200$. The former has the larger magnitude $|\omega_z|$ than the latter. Furthermore, the maximum deviates from the z axis. It is confirmed in Fig. 6 that the flow field has no spatial symmetry. It must be noted that only the traces of the maxima and (local) minima of ω_z which appear at $\mathrm{Re} = 60$ are drawn in Fig. 6, and the minima of ω_z having larger negative values emerge in the boundary layer near the side wall for $\mathrm{Re} > 260$. At $\mathrm{Re} = 285$, the locations of the maximum and local minima periodically oscillate in time because of the periodicity of the flow field. In Fig. 6, the locations of the maximum and local minima at which the y component of velocity v_1 peaks at its maximum and minimum values at $\mathrm{Re} = 285$ are indicated by 285 (max) and 285 (min), respectively. This shows the periodic oscillation of the bathtub vortex, which is characterized by the oscillatory movement of the center of the vortex.

B. Linear stability analysis

To prove that each transition of flow is certainly induced owing to instability of the flow having one more symmetries (basic flow) and lose one of them after transition, we numerically obtain the basic flow and examine the stability by solving the linear disturbance equation (10) at each Reynolds number necessary up to the second transition. The basic flow has the DPS for the first instability and the RS for the second, both of which are calculated with the SOR method or by numerical simulation imposing the corresponding symmetry, while the linear disturbance equation is solved with the numerical simulation method but using the normalization technique explained in Sec. II B.

Since the numerical simulation revealed that the first bifurcation occurs at $\mathrm{Re}_c^{\mathrm{I}} = 62.81$ and that the flow with the DPS loses both plane symmetries with respect to the $x = 0$ and $y = 0$ planes, only keeping the RS as seen in Figs. 3(c) and 3(d), we calculate the basic flow $(\bar{\boldsymbol{u}}, \bar{p})$ and examine its stability in $50 \leqslant \mathrm{Re} \leqslant 100$ across the critical value for the first instability.

The basic flow $(\bar{\boldsymbol{u}}, \bar{p})$ is qualitatively independent of Re in $50 \leqslant \mathrm{Re} \leqslant 100$ being similar to Figs. 3(a) and 3(b) for $\mathrm{Re} = 60$, so that we omit displaying the flow field to save space. Similarly, the basic flows around $\mathrm{Re}_c^{\mathrm{II}}$ and around $\mathrm{Re}_c^{\mathrm{III}}$ are qualitatively close enough to those at $\mathrm{Re} = 65$

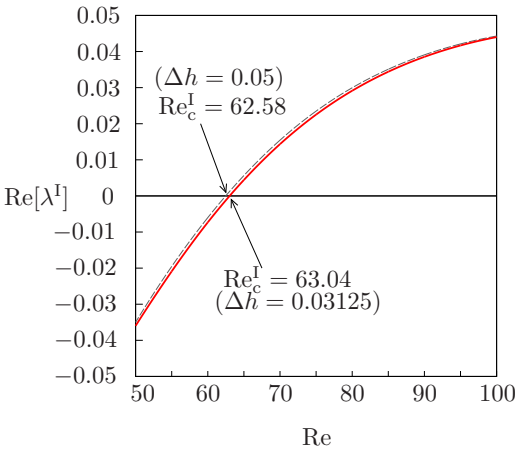

FIG. 7. Linear growth rate $\mathrm{Re}[\lambda^{\mathrm{I}}]$ of the most unstable mode of disturbance for double-plane symmetric flow.

[Figs. 3(c) and 3(d)] and at $\mathrm{Re} = 260$ [Figs. 3(e) and 3(f)], respectively. The linear stability analysis determines the linear growth rate, the oscillation frequency and the flow pattern of the most unstable mode of disturbance. The linear growth rate, $\mathrm{Re}[\lambda^{\mathrm{I}}]$, of the antisymmetric disturbance added to the double-plane symmetric flow is evaluated and shown in Fig. 7, where the eigen value is determined to be real ($\mathrm{Im}[\lambda^{\mathrm{I}}] = 0$). The linear growth rate $\mathrm{Re}[\lambda^{\mathrm{I}}]$ changes its sign at $\mathrm{Re} = 63.04$, showing that the double-plane symmetric flow is stable for $\mathrm{Re} < 63.04$ and unstable for $\mathrm{Re} > 63.04$. This threshold value is nothing but the critical Reynolds number $\mathrm{Re}_{\mathrm{c}}^{\mathrm{I}}$ at which the first bifurcation occurred in the numerical simulation. The coincidence of the values supports the validity of the linear stability analysis and the numerical simulation, where the critical Reynolds number is 62.81 (see Fig. 2), and the relative error between the two values is smaller than 0.4%.

Here, we demonstrate how the flow field loses the DPS owing to the growth of antisymmetric disturbance added to the symmetric basic flow field as a perturbation. Here, the antisymmetry of the disturbance means the reflection antisymmetry with respect to the planes of $x = 0$ and $y = 0$, which is expressed for the eigen functions, $\tilde{\boldsymbol{u}}^{\mathrm{I}}$ and $\tilde{p}^{\mathrm{I}}$, as

$$\tilde{u}^{\mathrm{I}}(x,y,z) = -\tilde{u}^{\mathrm{I}}(x,-y,z) = \tilde{u}^{\mathrm{I}}(-x,y,z), \tag{15a}$$

$$\tilde{v}^{\mathrm{I}}(x,y,z) = \tilde{v}^{\mathrm{I}}(x,-y,z) = -\tilde{v}^{\mathrm{I}}(-x,y,z), \tag{15b}$$

$$\tilde{w}^{\mathrm{I}}(x,y,z) = \tilde{w}^{\mathrm{I}}(x,-y,z) = \tilde{w}^{\mathrm{I}}(-x,y,z), \tag{15c}$$

$$\tilde{p}^{\mathrm{I}}(x,y,z) = \tilde{p}^{\mathrm{I}}(x,-y,z) = \tilde{p}^{\mathrm{I}}(-x,y,z). \tag{15d}$$

The z component of vorticity $\tilde{\omega}_z^{\mathrm{I}}$ on the $z = 1/2$ plane evaluated from the eigen function $\tilde{\boldsymbol{u}}^{\mathrm{I}}$ corresponding to the most unstable mode is shown in Fig. 8 for $\mathrm{Re} = 65$ as an example of Re around $\mathrm{Re}_{\mathrm{c}}^{\mathrm{I}} = 63.04$. The flow field given by the eigen function has three large-vorticity regions: one appearing along the z axis is composed of a sole bathtub vortex, and the other two near $(x,y) = (0,\pm 3/4)$ have the sign opposite to the bathtub vortex. Besides the three vortices, the flow field includes three intense vorticity regions near each side wall at $y = \pm 3/2$. The one near $x = 0$ has relatively strong vorticity of the same sign as the bathtub vortex, while the sign of vorticity in the pairs away from $x = 0$ is opposite to the bathtub vortex. Figure 8 clearly shows the DPS of $\tilde{\omega}_z^{\mathrm{I}}$, which comes from the antisymmetry of the velocity field of the eigen function with respect to the planes of $x = 0$ and $y = 0$ shown by Eq. (15). The double plane antisymmetry of the eigen function is interpreted as the composition of the RS and one of the plane antisymmetries with respect to the $x = 0$ and $y = 0$ planes. Since the velocity field in the bifurcated flow is given as the sum of the

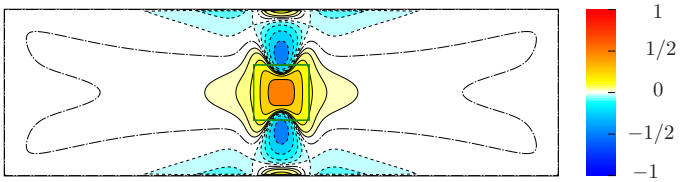

FIG. 8. Contours of z-component vorticity of the linear eigen function on the $z = 1/2$ plane. Re $= 65$. The vorticity is normalized so that its maximum is unity. The contours are drawn for $\tilde{\omega}_z^{\mathrm{I}} = \pm 2^{-n}$, where $n = 1, \ldots, 5$ and $\tilde{\omega}_z^{\mathrm{I}} = 0$. The solid lines, dashed lines, and dashed-dotted lines, respectively, represent positive $\tilde{\omega}_z^{\mathrm{I}}$, negative $\tilde{\omega}_z^{\mathrm{I}}$, and zero $\tilde{\omega}_z^{\mathrm{I}}$.

basic flow and the disturbance, and the basic flow has the RS and one of the plane symmetries with respect to the $x = 0$ plane and the $y = 0$ plane, the resultant flow after instability retains only the RS, being common to the basic flow and the disturbance.

Since the DPS flow has no total angular momentum in the z direction L_z, the most unstable mode of disturbance produces L_z to yield the bathtub vortex. The physical mechanism to induce L_z comes from the flow structure of the mode of disturbance. In the linear stability analysis, the growth rate of L_z is also Re$[\lambda^{\mathrm{I}}]$ and the growth Re$[\lambda^{\mathrm{I}}]L_z$ is expressed by the sum of torques due to pressure and viscous friction on the walls or the bottom of the container together with the angular momentum supply from the outside. The torques due to pressure on the side walls perpendicular to the x and y axes are, respectively, denoted by $N_{\mathrm{p}x}$ and $N_{\mathrm{p}y}$, where the first suffix p attached to N stands for pressure and the second suffix x or y indicates the normal axis of the solid boundaries on which the torque is exerted on water in the container. It is added that the torque due to pressure on the bottom $N_{\mathrm{p}z}$ makes no contribution on L_z. The viscous force always acts to reduce L_z, and the torques due to the viscous force on the walls and the bottom are expressed as $N_{\mathrm{v}x}$, $N_{\mathrm{v}y}$, and $N_{\mathrm{v}z}$, respectively. The angular momentum supply Q_{in} flowing in from the inlet sections vanishes by the inflow condition, and the outflow of the angular momentum through the outlet Q_{out} contributes to reduce L_z.

Because the DPS of the basic flow does not make the torques due to the pressure and the viscous friction as well as L_z, the angular momentum budget due to the most unstable mode of disturbance is evaluated here. Each torque is calculated by integrals over the walls. For instance, $\tilde{N}_{\mathrm{p}y}^{\mathrm{I}}$ is expressed as

$$\tilde{N}_{\mathrm{p}y}^{\mathrm{I}} = -\iint_{\mathrm{S}_{y+}} x\,\tilde{p}^{\mathrm{I}}(x,y,z)dxdz + \iint_{\mathrm{S}_{y-}} x\,\tilde{p}^{\mathrm{I}}(x,y,z)dxdz = -2\iint_{\mathrm{S}_{y+}} x\,\tilde{p}^{\mathrm{I}}(x,y,z)dxdz, \quad (16)$$

where S_{y+} (S_{y-}) indicates the areas of the side walls at $y = 3/2$ for $z > 0$ and $y = 1/2$ for $z < 0$ ($y = -3/2$ for $z > 0$ and $y = -1/2$ for $z < 0$). We used the relation of the π-rotational symmetry of the flow field; $\tilde{p}^{\mathrm{I}}(x,y,z)$ on S_{y+} equals to $\tilde{p}^{\mathrm{I}}(-x,y,z)$ on S_{y-}. Similarly, the torque due to the viscous stress on the bottom is defined as

$$\tilde{N}_{\mathrm{v}z}^{\mathrm{I}} = \frac{1}{\mathrm{Re}}\iint_{\mathrm{S}_z}\left(-x\frac{\partial \tilde{v}^{\mathrm{I}}}{\partial z} + y\frac{\partial \tilde{p}^{\mathrm{I}}}{\partial z}\right)dxdy, \quad (17)$$

in which S_z denotes the area of the bottom at $z = 0$ outside the drain hole. The conservation law of the angular momentum leads the following equation:

$$\mathrm{Re}[\lambda^{\mathrm{I}}]\tilde{L}_z^{\mathrm{I}} = \tilde{Q}_{\mathrm{in}}^{\mathrm{I}} + \left(-\tilde{Q}_{\mathrm{out}}^{\mathrm{I}}\right) + \tilde{N}_{\mathrm{p}x}^{\mathrm{I}} + \tilde{N}_{\mathrm{p}y}^{\mathrm{I}} + \tilde{N}_{\mathrm{v}x}^{\mathrm{I}} + \tilde{N}_{\mathrm{v}y}^{\mathrm{I}} + \tilde{N}_{\mathrm{v}z}^{\mathrm{I}}, \quad (18)$$

where $\mathrm{Re}[\lambda^{\mathrm{I}}]\tilde{L}_z^{\mathrm{I}}$ corresponds to the temporal derivative of $\tilde{L}_z^{\mathrm{I}}$. The outflow $\tilde{Q}_{\mathrm{out}}^{\mathrm{I}}$ is positive having the same sign with the induced angular momentum $\tilde{L}_z^{\mathrm{I}}$, and hence the contribution of $(-\tilde{Q}_{\mathrm{out}}^{\mathrm{I}})$ to the growth of $\tilde{L}_z^{\mathrm{I}}$ is negative.

TABLE III. Angular momentum budget due to eigen function $\tilde{\boldsymbol{u}}^{\mathrm{I}}$ and $\tilde{p}^{\mathrm{I}}$ at Re = 65.

$\tilde{L}^{\mathrm{I}}_z$	$-\tilde{Q}^{\mathrm{I}}_{\mathrm{out}}$	$\tilde{N}^{\mathrm{I}}_{\mathrm{p}x}$	$\tilde{N}^{\mathrm{I}}_{\mathrm{p}y}$	$\tilde{N}^{\mathrm{I}}_{\mathrm{v}x}$	$\tilde{N}^{\mathrm{I}}_{\mathrm{v}y}$	$\tilde{N}^{\mathrm{I}}_{\mathrm{v}z}$	$\mathrm{Re}[\lambda^{\mathrm{I}}]\tilde{L}^{\mathrm{I}}_z$
7.952	-5.825×10^{-8}	−0.1887	1.3038	−0.2636	−0.2543	−0.5564	4.080×10^{-2}

The angular momentum $\tilde{L}^{\mathrm{I}}_z$, all the torques $\tilde{N}^{\mathrm{I}}_{\mathrm{p}x}$, $\tilde{N}^{\mathrm{I}}_{\mathrm{p}y}$, $\tilde{N}^{\mathrm{I}}_{\mathrm{v}x}$, $\tilde{N}^{\mathrm{I}}_{\mathrm{v}y}$, $\tilde{N}^{\mathrm{I}}_{\mathrm{v}z}$ and the outflow $\tilde{Q}^{\mathrm{I}}_{\mathrm{out}}$ of $\tilde{L}^{\mathrm{I}}_z$ are evaluated from the eigen function $(\tilde{\boldsymbol{u}}^{\mathrm{I}}, \tilde{p}^{\mathrm{I}})$ and tabulated in Table III for Re = 65, where the eigen function is normalized to be $\tilde{v}^{\mathrm{I}}_1 = 1$ to uniquely define the magnitude and the phase, and Simpson's formula is used for numerical integrations. The normalization of $\tilde{v}^{\mathrm{I}}_1$ gives positive value of $\tilde{L}^{\mathrm{I}}_z$ as listed in Table III. The torques $\tilde{N}^{\mathrm{I}}_{\mathrm{v}x}$, $\tilde{N}^{\mathrm{I}}_{\mathrm{v}y}$, and $\tilde{N}^{\mathrm{I}}_{\mathrm{v}z}$ due to the viscous stresses on the side walls and the bottom have negative values, because the viscous stresses act to resist the vortical motion. The only acceleration of $\tilde{L}^{\mathrm{I}}_z$ is brought by the pressure on the side walls normal to the y axis, $\tilde{N}^{\mathrm{I}}_{\mathrm{p}y}$, and the pressure on the side walls normal to the x axis, $\tilde{N}^{\mathrm{I}}_{\mathrm{p}x}$, works against the vortical motion. Thus, the eigen function indicates that the pressure torque on the side walls normal to the y direction causes the bathtub vortex. The origin of the torque is consistent with the numerical simulations in Ref. [18]. The outflow $\tilde{Q}^{\mathrm{I}}_{\mathrm{out}}$ evaluated in the linear stability analysis is much smaller than that in the numerical simulations even after taking the normalization into consideration, because such an intensified outflow $\tilde{Q}^{\mathrm{I}}_{\mathrm{out}}$ is caused by the nonlinearity.

As clarified in Ref. [18], the torque due to pressure on the side walls is the only driving mechanism that accelerates the bathtub vortex at $\mathrm{Re} > \mathrm{Re}^{\mathrm{I}}_{\mathrm{c}}$. The torque density on the side walls due to the pressure disturbance around $\mathrm{Re} = \mathrm{Re}^{\mathrm{I}}_{\mathrm{c}}$ is defined as $\tilde{n}^{\mathrm{I}}_{\mathrm{p}y}(x,\pm3/2,z) = \mp x\,\tilde{p}^{\mathrm{I}}(x,\pm3/2,z)$, which is drawn in Fig. 9 for Re = 65, though this figure is almost the same as that given in Ref. [18]. The torque density at such Re is identical on both side walls normal to the y axis, since the pressure disturbance has the reflection antisymmetry [Eq. (15d)]. It is clarified that the strongest torque is brought by the existence of the two intense small vortices close to the side walls, when Fig. 9 is compared with Fig. 8. The non-negativity in the torque distribution over the entire areas of the side walls confirms the fact that the torque due to pressure certainly drives the bathtub vortex.

The flow bifurcated owing to instability of the basic flow, possessing the RS, will also experience instability, which becomes the basic flow for the next stability analysis in turn. The RS flow is obtained by the numerical simulation of Eq. (1) under the π-rotation symmetry condition or with the SOR method similarly to the basic flow having the DPS. The flow patterns of the RS flow are similar to that at Re = 65 depicted in Figs. 3(c) and 3(d) qualitatively independent of Re, so that

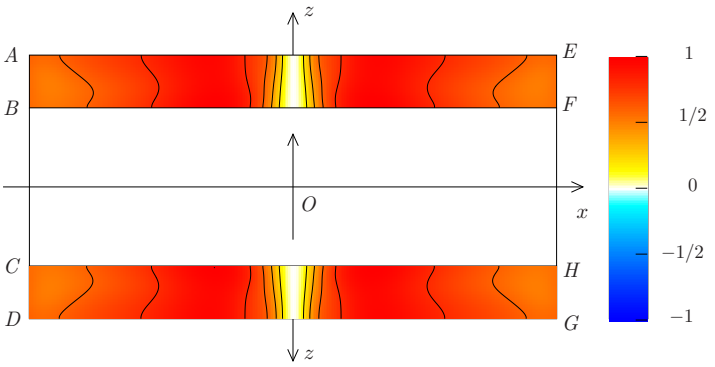

FIG. 9. Torque density due to the pressure disturbance on the side walls $\tilde{n}^{\mathrm{I}}_{\mathrm{p}y}$ on $y = 3/2$ (top) and $y = -3/2$ (bottom) at Re = 65. The torque density is normalized so that its maximum is unity. Contours are drawn for every 0.2.

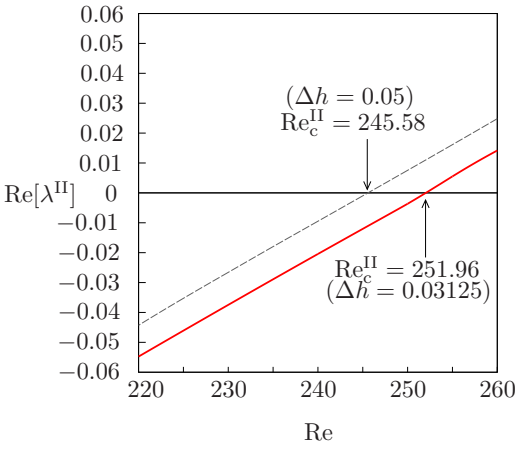

FIG. 10. Linear growth rate $\mathrm{Re}[\lambda^{\mathrm{II}}]$ of the most unstable mode of disturbance for the π-rotational symmetric (RS) flow.

we omit them to save space. The linear growth rate, $\mathrm{Re}[\lambda^{\mathrm{II}}]$, of disturbance added to the RS flow is shown in Fig. 10. Here, the eigen value has a real value again. The linear growth rate changes its sign from negative to positive across $\mathrm{Re} = 251.96$. The threshold value is close to the critical Reynolds number at the second bifurcation identified in the numerical simulations, $\mathrm{Re}_{\mathrm{c}}^{\mathrm{II}} = 251.01$. Thus, this supports the instability and bifurcation of the RS flow at $\mathrm{Re} > \mathrm{Re}_{\mathrm{c}}^{\mathrm{II}}$.

The eigen function is displayed by using $\tilde{\omega}_z^{\mathrm{II}}$ on the plane of $z = 1/2$ for $\mathrm{Re} = 260$ ($\approx \mathrm{Re}_{\mathrm{c}}^{\mathrm{II}}$) in Fig. 11. The vorticity distribution $\tilde{\omega}_z^{\mathrm{II}}$ is clearly different from $\tilde{\omega}_z^{\mathrm{I}}$, both positive and negative signs appearing near the z axis, and a pair of relatively large-vorticity regions having opposite sign extend from the side walls over the edge of the drain hole. It is noticeable that the $\tilde{\omega}_z^{\mathrm{II}}$ distribution has the π-rotational *antisymmetry* around the z axis, which is caused by the π-rotational antisymmetric distribution of velocity in the eigen function. The velocity distribution is invariant under the composition of the π-rotation operation around the z axis $R_{z\pi}$ and the sign inversion for the horizontal components of velocity:

$$\begin{aligned} \tilde{u}^{\mathrm{II}}(x,y,z) &= \tilde{u}^{\mathrm{II}}(-x,-y,z), \quad \tilde{v}^{\mathrm{II}}(x,y,z) = \tilde{v}^{\mathrm{II}}(-x,-y,z), \\ \tilde{w}^{\mathrm{II}}(x,y,z) &= \tilde{w}^{\mathrm{II}}(-x,-y,z), \quad \tilde{p}^{\mathrm{II}}(x,y,z) = \tilde{p}^{\mathrm{II}}(-x,-y,z). \end{aligned} \tag{19}$$

Since the π-rotational antisymmetric disturbance is added to the basic flow with the RS, the resultant flow has no spatial symmetry at all.

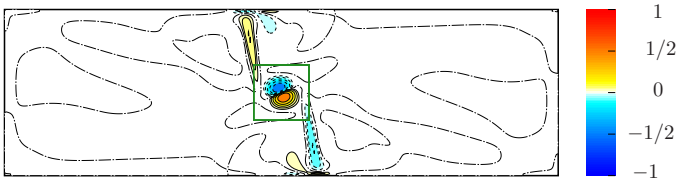

FIG. 11. Contours of z-component vorticity of the linear eigen function on the $z = 1/2$ plane. $\mathrm{Re} = 260$. The vorticity is normalized so that its maximum is unity. The contours are drawn for $\tilde{\omega}_z^{\mathrm{II}} = \pm 2^{-n}$, where $n = 1, \ldots, 5$, and $\tilde{\omega}_z^{\mathrm{II}} = 0$. The solid lines, dashed lines, and dashed-dotted lines, respectively, represent positive $\tilde{\omega}_z^{\mathrm{II}}$, negative $\tilde{\omega}_z^{\mathrm{II}}$, and zero $\tilde{\omega}_z^{\mathrm{II}}$.

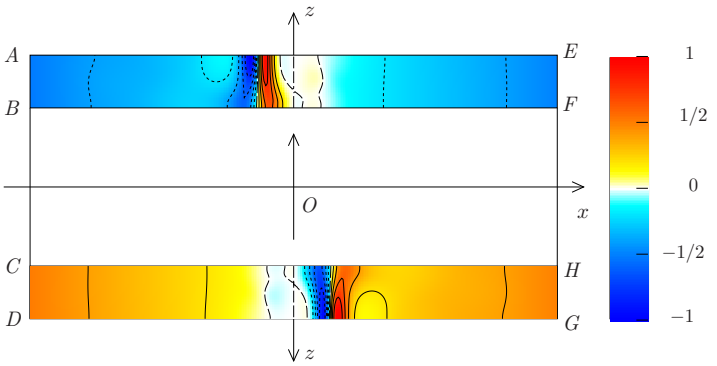

FIG. 12. Torque density due to the pressure disturbance on the side walls $\tilde{n}^{\mathrm{II}}_{py}$ on $y = 3/2$ (top) and $y = -3/2$ (bottom) for $\mathrm{Re} = 260$ slightly larger than $\mathrm{Re}^{\mathrm{II}}_{\mathrm{c}}$. The torque density is normalized so that its maximum is unity. Contours are drawn for every 0.2.

The torque density on the side walls due to the pressure disturbance around $\mathrm{Re} = \mathrm{Re}^{\mathrm{II}}_{\mathrm{c}}$ is defined as $\tilde{n}^{\mathrm{II}}_{py}(x,\pm 3/2,z) = \mp x\,\tilde{p}^{\mathrm{II}}(x,\pm 3/2,z)$, and is depicted in Fig. 12. The torque density distributions on the side walls at $y = \pm 3/2$ also show the π-rotational antisymmetry, resulting from that of the pressure disturbance. Because of the π-rotational antisymmetry, the integration of the torque density due to the pressure disturbance over the two side walls at $y = \pm 3/2$ vanishes, and hence the torque $\tilde{n}^{\mathrm{II}}_{py}$ makes no contribution in driving the bathtub vortex. It is also of interest to point out that the locations of the large magnitudes of the torque shown in Fig. 12 are close to the root of the fingerlike structure of the large magnitudes of the vorticity in Fig. 11.

The numerical accuracy of the linear stability analysis is verified by the comparison of the two critical Reynolds numbers, $\mathrm{Re}^{\mathrm{I}}_{\mathrm{c}}$ and $\mathrm{Re}^{\mathrm{II}}_{\mathrm{c}}$ for different grid spacings Δh and time steps Δt in Table IV, where the critical Reynolds numbers obtained in the numerical simulations are also included. The relative error in $\mathrm{Re}^{\mathrm{II}}_{\mathrm{c}}$ between the analyses with $\Delta h = 0.05$ and those with $\Delta h = 0.03125$ is smaller than 2.6%, so that the grid spacing $\Delta h = 0.03125$ is verified to give sufficient accuracy in the linear stability analysis for the second instability.

IV. SUMMARY AND DISCUSSION

We have investigated the transitions of flow induced when water is drained from the vessel that has the double plane symmetry with respect to the two vertical planes of $x = 0$ and $y = 0$ (DPS) by numerical simulations and linear stability analyses. It was found that the flow experiences three transitions in the range of $\mathrm{Re} \leqslant 300$, and the critical Reynolds numbers for the occurrences of transitions were determined. The transitions were discussed in terms of symmetries that the flow field

TABLE IV. Accuracy assessment of the linear stability analysis. The critical Reynolds numbers of the first and second bifurcation evaluated in the linear stability analyses together with numerical simulation results. The relative errors ϵ are based on the values from the linear stability analysis with $\Delta h = 0.03125$.

		Linear stability analysis		Numerical simulation	
Δh	Δt	$\mathrm{Re}^{\mathrm{I}}_{\mathrm{c}}$	$\mathrm{Re}^{\mathrm{II}}_{\mathrm{c}}$	$\mathrm{Re}^{\mathrm{I}}_{\mathrm{c}}$	$\mathrm{Re}^{\mathrm{II}}_{\mathrm{c}}$
0.03125	2×10^{-3}	63.04	251.96	62.81	251.01
ϵ	–	–	–	0.36%	0.38%
0.05	5×10^{-3}	62.58	245.58	62.24	245.25
ϵ	–	0.73%	2.5%	1.3%	2.7%

possesses before and after each transition. It was clarified that the flow field becomes more complex loosing one symmetry in each transition, i.e., in each experience of instability. The spatial symmetry is broken by the disturbance having an antisymmetry corresponding to each lost symmetry in the two pitchfork bifurcations. The time-translation symmetry is broken by the time-periodic disturbance in the Hopf bifurcation.

In the present study, for $\mathrm{Re} < \mathrm{Re}_c^{\mathrm{I}}$ (the value of $\mathrm{Re}_c^{\mathrm{I}}$ is 62.81 in the numerical simulation and 63.04 in the linear stability analysis), a unique solution exists. The flow that the unique solution gives has the same DPS as the system's configuration, and no bathtub vortex emerges. The DPS is interpreted as the composition of the π-rotational (twofold) symmetry with respect to the z axis (RS) and one of the plane symmetries with respect to the $x = 0$ and $y = 0$ planes.

At $\mathrm{Re} = \mathrm{Re}_c^{\mathrm{I}}$, two solutions emerge from the unique solution owing to a pitchfork bifurcation. At the bifurcation, the most unstable mode of disturbance has the reflection antisymmetry with respect to the $x = 0$ and $y = 0$ planes as well as the RS. Therefore, the superposition of the disturbance on the basic flow gives rise to flows that has the RS, reducing the plane symmetries. The resultant flow with the RS becomes possessed of a steady bathtub vortex swirling in either direction for $\mathrm{Re}_c^{\mathrm{I}} < \mathrm{Re}$ ($<\mathrm{Re}_c^{\mathrm{II}}$), and the center axis of the bathtub vortex coincides with that of the drain hole.

At $\mathrm{Re} = \mathrm{Re}_c^{\mathrm{II}}$ (251.01 in the numerical simulation and 251.96 in the linear stability analysis), the two solutions bifurcate into four solutions owing to another pitchfork bifurcation. At $\mathrm{Re}_c^{\mathrm{II}}$, the RS is broken by the most unstable disturbance having the π-rotational antisymmetry. The resultant flow loses all the spatial symmetries for $\mathrm{Re} > \mathrm{Re}_c^{\mathrm{II}}$, and the center axis of the bathtub vortex migrates away from the center axis of the drain hole.

The three kinds of flow in the range of $\mathrm{Re} < \mathrm{Re}_c^{\mathrm{III}}$ (278.0 in the numerical simulation with the coarser grid) are steady, having time-translation symmetry. However, the time-translation symmetry of the flow is broken by instability due to a time-periodic disturbance at $\mathrm{Re} = \mathrm{Re}_c^{\mathrm{III}}$ via a Hopf bifurcation. For $\mathrm{Re} > \mathrm{Re}_c^{\mathrm{III}}$, the center and the strength of the bathtub vortex periodically oscillate in the oscillation-induced flow.

Similarly to dynamical systems of much fewer degrees of freedom, it has been shown that the transitions of flow accompany symmetry-breaking in each: the breaking of one of the two plane symmetries with respect to the $x = 0$ and $y = 0$ planes being followed by the other plane symmetry, that of the π-rotational symmetry around the center axis of the drain hole, and that of the time-translation symmetry. The flow will eventually become fully turbulent through further finite or infinite times of transitions. Thus the model treated in the present paper shows a typical transition route to turbulence for a wider class of flows which have two plane symmetries. This model flow also provides one of examples in which large-scale vortical motion is induced by instability like the Kelvin-Helmholtz instability. The Kelvin-Helmholtz instability occurs in two counter streams passing each other, while the present model shows that a large vortex appears owing to instability of two colliding streams.

We adopted one single configuration where the drain hole is located at the center of the bottom, the length ratio of the horizontal cross section is $a/b = 10/3$, and the side length of the drain hole is only one third of the shorter side of the vessel, $d = b/3$. The critical Reynolds number evaluated in the present paper is as small as $\mathrm{Re}_c^{\mathrm{I}} \approx 63$, since the ratio of the side length of the drain hole to the shorter side wall is as large as $1/3$. The critical value is anticipated to be much larger for smaller ratios as the cases of real bathtubs or wash balls. For example, $\mathrm{Re}_c^{\mathrm{I}} = O(10^3)$ in Ref. [17], though the shape of the cross section of the vessel is not exactly rectangular because of the inclusion of a hexagonal percolator in the central region in the experiment. The length scale ratio of the horizontal cross section is also crucial to determine the critical value, and the pitchfork bifurcation will never happen for smaller length ratios according to our preliminary numerical calculations, which will be published elsewhere.

We have not considered the Earth's rotation effect. If the experimental apparatus is placed on a rotational base like on the Earth, the rotation makes the first bifurcation to be imperfect. In the imperfect pitchfork bifurcation (Fig. 13), one of the solution branches is continuous starting from

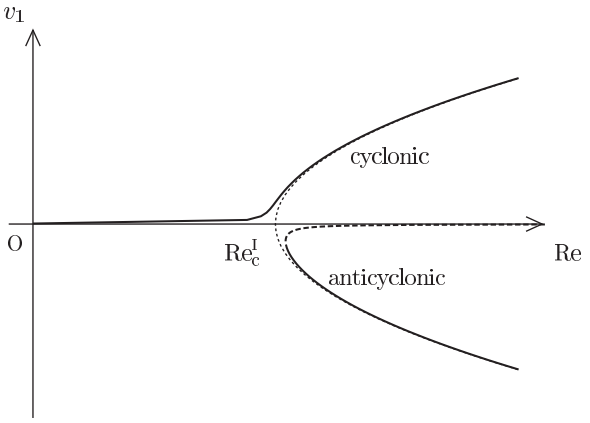

FIG. 13. Imperfect pitchfork bifurcation diagram reduced by a rotation effect. Solid lines: stable, dashed line: unstable, dotted line: perfect pitchfork bifurcation.

$\mathrm{Re} = 0$, so that the cyclonic solution is chosen even by a slow angular velocity of rotation. Hence the swirl direction is to be cyclonic as shown in our previous paper [18]. As seen in Fig. 13 the anticyclonic vortex is possible if some disturbance is added, so that the solution may jump from the cyclonic solution branch to the anticyclonic one. The Earth's rotation does not cause the structural instability at the second bifurcation because the basic flow has the RS and the Coriolis force does not break the RS. That is, the second bifurcation is still a pitchfork bifurcation even if the Coriolis force is introduced. Because Hopf bifurcations are structurally stable, the Earth's rotation change neither the third bifurcation structure.

One may have a concern with the assumption of the flat surface in the bathtub-vortex flow. It is apparent that that the linear stability at $\mathrm{Re}_c^{\mathrm{I}}$ is not affected by the assumption because the magnitude of the bathtub vortex is too small to affect the water surface. For larger Reynolds numbers than $\mathrm{Re}_c^{\mathrm{I}}$, the dip on the surface Δd in terms of dimensional variables, if the surface displacement were allowed, is estimated roughly by the ratio of $\rho g \Delta d$ to ρu_θ^2 with the gravity acceleration g and the circumferential velocity of the bathtub vortex u_θ. The circumferential velocity can be kept negligibly small if the Froude number $\mathrm{Fr} = Q/\sqrt{gd^5}$ is small enough.

As stated in the introduction, we do not limit our interest to the flows in real bathtubs, but are interested in the model flow having the double-plane symmetry for which we found sequential transitions up to the third, where the flow is complex and time periodic. However, the effect of the surface deformation on the bathtub vortex is also an interesting subject of investigation because the deformation may alter the transitions for larger Froude numbers. It is added that the depth of dip on the water surface was measured in experiments and predicted analytically [19] and also evaluated by applying a modified Lundgren model [5].

ACKNOWLEDGMENTS

The authors thank Ms. Sachie Hayashi and Ms. Rei Matsuda for helping preparation of the figures. This work was partially supported by JSPS KAKENHI Grant No. JP15K05220, No. JP15K17971, and No. JP16K05490.

[1] A. H. Shapiro, Bath-tub vortex, Nature **196**, 1080 (1962).
[2] L. M. Trefethen, R. W. Bilger, P. T. Fink, R. E. Luxton, and R. I. Tanner, The bath-tub vortex in the southern hemisphere, Nature **207**, 1084 (1965).

[3] M. Sibulkin, A note on the bathtub vortex, J. Fluid Mech. **14**, 21 (1962).
[4] D. L. Kelly, B. W. Martin, and E. S. Taylor, A further note on the bathtub vortex, J. Fluid Mech. **19**, 539 (1964).
[5] Y. A. Stepanyants and G. H. Yeoh, Stationary bathtub vortices and a critical regime of liquid discharge, J. Fluid Mech. **604**, 77 (2008).
[6] J. R. Weske, On the origin and mechanism of vortex motion at the inlet of intakes placed near a flat surface, University of Maryland, Tech. Note BN-152, AFOSR-TN-58, 863 (1958).
[7] T. S. Lundgren, The vortical flow above the drain-hole in a rotating vessel, J. Fluid Mech. **155**, 381 (1985).
[8] A. Y. Klimenko, Moderately strong vorticity in a bathtub-type flow, Theoret. Computat. Fluid Dynam. **14**, 243 (2001).
[9] A. Andersen, T. Bohr, B. Stenum, J. J. Rasmussen, and B. Lautrup, The bathtub vortex in a rotating container, J. Fluid Mech. **556**, 121 (2006).
[10] P. A. Tyvand and K. B. Haugen, An impulsive bathtub vortex, Phys. Fluids **17**, 062105 (2005).
[11] N. Yokoyama, Y. Maruyama, and J. Mizushima, Origin of the bathtub vortex and its formation mechanism, J. Phys. Soc. Jpn. **81**, 074401 (2012).
[12] L. Bøhling, A. Andersen, and D. Fabre, Structure of a steady drain-hole vortex in a viscous fluid, J. Fluid Mech. **656**, 177 (2010).
[13] J. D. Crawford and E. Knobloch, Symmetry and symmetry-breaking bifurcations in fluid dynamics, Annu. Rev. Fluid Mech. **23**, 341 (1991).
[14] Y. A. Kuznetsov, *Elements of Applied Bifurcation Theory*, 3rd ed. (Springer, Berlin, 2004).
[15] R. B. Hoyle, *Pattern Formation: An Introduction to Methods* (Cambridge University Press, Cambridge, 2006).
[16] S. Shingubara and T. Kawakubo, Formation of vortices around a sinkhole, J. Phys. Soc. Jpn. **53**, 1026 (1984).
[17] T. Kawakubo, Y. Tsuchiya, M. Sugaya, and K. Matsumura, Formation of a vortex around a sink: A kind of phase transition in a nonequilibrium open system, Phys. Lett. A **68**, 65 (1978).
[18] J. Mizushima, K. Abe, and N. Yokoyama, Bathtub vortex induced by instability, Phys. Rev. E **90**, 041002 (2014).
[19] B. T. Lubin and G. S. Springer, The formation of a dip on the surface of a liquid draining from a tank, J. Fluid Mech. **29**, 385 (1967).